PAPER

Check for updates

Facile synthesis of novel NH₂-MIL-53(Fe)/AgSCN heterojunction composites as a highly efficient photocatalyst for ciprofloxacin degradation and H₂ production under visible-light irradiation

Jungang Yi,[†][a] Xianghui Wu,[†][a] Huadong Wu,[a] Jia Guo,[a]
Kun Wu[ab] and Linfeng Zhang ![iD] *[ac]

With the aim of solving the increasingly serious problem of environmental pollution and the energy crisis, in this work a novel NH₂-MIL-53(Fe)/AgSCN (NMFA) composite photocatalyst was successfully prepared through a one-step chemical precipitation method. The prepared composites demonstrate an excellent photocatalytic performance for ciprofloxacin (CIP) and rhodamine B (RhB) degradation under visible-light irradiation. Within 60 min, the degradation rate for CIP and RhB reached 90% and 100%, respectively, which was 1.84/3.33 times and 1.79/2.04 times greater than that of the single NH₂-MIL-53(Fe) and AgSCN samples. Furthermore, the H₂ production rate of the NMFA-5 composite was 4742 μmol g^{-1} h^{-1}, which was 5.25 and 17.37 times greater than that of the pure samples. Owing to the combination of NH₂-MIL-53(Fe) and AgSCN, the separation and transmission efficiency of the photon-generated carriers in the composites was improved, which was demonstrated using optical characterization and a series of electrochemical characterization techniques. In addition, a possible mechanism for the excellent photocatalytic performance of the NMFA composites is discussed. The work in this paper may provide a technical reference for the application of silver modified metal organic frameworks (MOFs)-based composite photocatalysts for the treatment of environmental remediation.

1 Introduction

The environment has been extensively damaged by rapid changes in the way humans live, resulting in soil, atmospheric and water pollution.[1–3] Specifically, industrial sewage containing organic dyes and antibiotics is a particularly problematic form of pollution owing to the structural stability and low concentration of the pollutants. Many technological advances have focused on dealing with this problem, such as the physical–chemical precipitation method, membrane separation method, adsorption method, biodegradation method, ultrafiltration and reverse osmosis

techniques, and so on.[4–8] Nevertheless, there are many disadvantages to these methods, such as a lack of complete degradation, weak selectivity, high costs, complicated operation, and the formation of secondary pollutants. Therefore, finding an efficient technique to deal with these pollutants that is cheap, easy to operate and environment friendly is urgently needed and would be of great significance. On the other hand, air pollution can be caused by CO, CO_2, SO_2 and other gases, resulting from the burning of fossil fuels and coal and emissions from motor vehicle exhaust fumes.[9,10] Therefore, finding a clean and sustainable energy source can not only avoid environmental pollution, but also be an important means to solve the energy crisis. The higher calorific value and clean final product (H_2O) of H_2 fuel has been highly praised by scientists, and it is deemed to be one of the most ideal novel energy sources.[11] For example, the electrolysis of water, the biological enzyme method and the photocatalytic water splitting method have been used for the treatment of sewage.[12–14] The photocatalytic H_2 emission reaction (HER) accomplished by water decomposition is regarded as the most economical method of water splitting.[15]

Photocatalytic technology has resulted in major achievements in the treatment of water, energy development

[a] *Key Laboratory for Green Chemical Process of Ministry of Education, Hubei Key Laboratory of Novel Reactor and Green Chemical Technology, School of Chemical Engineering and Pharmacy, Wuhan Institute of Technology, Wuhan 430205, People's Republic of China. E-mail: guojia@wit.edu.cn, lfzhang@wit.edu.cn; Fax: +86 027 87194980, Fax: +86 027 87905262*
[b] *The College of Post and Telecommunication of Wuhan Institute of Technology, Wuhan 430073, People's Republic of China*
[c] *School of Chemical Engineering and Technology, Tianjin University, Tianjin 300072, PR China*
† These authors contributed equally to this work and should be considered co-first authors.

and N$_2$ fixation and reduction since the field of photocatalysis was first reported in 1972 by Fujishima.[16] In a recent report, Sun *et al.* synthesized Co/Bi composites using an *in situ* calcination process, which was used for the degradation of ciprofloxacin (CIP) under visible light.[17] In addition, Huang *et al.* successfully synthesized urchin-like CeO$_2$/ZnO@Au composite photocatalysts that can almost completely remove rhodamine B (RhB) from a sample within 20 min.[18] Chen *et al.* prepared novel Ag$_3$PO$_4$/P-g-C$_3$N$_4$ composites through a two-step chemical route, which enabled highly efficient photocatalytic hydrogen production.[19] Chen *et al.* prepared the novel Bi$_2$S$_3$/KTa$_{0.75}$Nb$_{0.25}$O$_3$ (KTN) and CuS/KTa$_{0.75}$Nb$_{0.25}$O$_3$ (KTN) heterojunction composites and applied them for N$_2$ fixation and reduction.[20,21] In short, photocatalysis is a green and efficient oxidation technology and has shown advantages such as a wide range of selectivity, the synthesis of green products under mild conditions, and a good recyclability. In particular, it has been widely used for the degradation of antibiotics and organic dye pollution (such as CIP and RhB), as well as to efficiently produce hydrogen at room temperature.

Recently, metal organic frameworks (MOFs), which are a combination of metal ions and organic ligands, have attracted widespread attention from scientists because of their large specific surface area, convenient processing techniques, simple synthesis and other features, such as the lack of pollution resulting from them.[22] As they contain a high energy density Fe–O bond, Fe-MOFs possess an excellent stability in organic solvents and water compared with other MOFs.[23] However, the Fe-MOFs still face challenges in practical applications owing to problems such as a low separation between the electrons and holes and the poor transfer efficiency. In order to solve this problem, the construction of heterostructure Fe-MOFs based composites with other semiconductors seems to be a feasible method. Among the various Ag-based materials, AgSCN has been reported to be an excellent photocatalyst because of its high structural stability and reasonable band gap structure. Therefore, the Fe-MOFs and AgSCN composites may improve the separation and transfer efficiency of the electrons and holes, effectively enhancing the photocatalytic performance of the composites.[24–26]

Herein, in this work a NH$_2$-MIL-53(Fe)/AgSCN (NMFA) composites photocatalyst was successfully prepared using a simple method, and the composites exhibited an excellent photocatalytic activity, successfully removing the CIP and RhB, and evolving H$_2$. The field emission scanning electron microscope (FESEM) and high resolution transmission electron microscopy (HRTEM) results indicated there is close contact between the NH$_2$-MIL-53(Fe) and AgSCN. Furthermore, the photoluminescence (PL), electrochemical impedance spectroscopy (EIS) and transient photocurrent response indicated that the separation and transfer efficiency of the photogenerated electrons and holes were improved by recombining a certain proportion of the AgSCN, therefore the

photocatalytic performance of the NMFA composites was significantly improved. The stability and recyclability of the NMFA composites was evaluated for five cycles. Quenching experiments and electron spin resonance (ESR) tests were used to detect the activity of the free radicals in the catalytic process. Furthermore, the possible photocatalytic mechanism of degradation and H$_2$ evolution of the NMFA composites were discussed, respectively.

2 Experimental

2.1 Reagents

All chemicals were commercially available and of analytical grade, they were used without further purification. Sodium thiocyanate (NaSCN), silver nitrate (AgNO$_3$), 2-aminoterephthalic acid (NH$_2$-BDC), CIP and RhB were purchased from Aladdin. Chloroplatinic acid (H$_2$PtCl$_6$), iron(III) chloride hexahydrate (FeCl$_3$·6H$_2$O), triethanolamine (TEOA), eosin Y (EY), *N,N*-dimethyl-formamide (DMF), hydrogen peroxide (30%, v/v), ethylenediaminetetraacetic acid disodium salt (EDTA-2Na), isopropyl alcohol (IPA), ascorbic acid (AC) and ethanol (EtOH) were all purchased from Sinopharm Chemical Reagent Co., Ltd (China).

2.2 Synthesis of the NMFA composites

2.2.1 Synthesis of NH$_2$-MIL-53(Fe). NH$_2$-MIL-53(Fe) was prepared using the solvothermal method. Typically, 2 mmol of NH$_2$-BDC and 2 mmol of FeCl$_3$·6H$_2$O were dissolved in 42 mL of DMF. After stirring uniformly at room temperature, the solution was transferred to a Teflon-lined auto-clave and kept at 150 °C for 3 h. Upon cooling to ambient temperature, the slurry was vacuum filtered to obtain a brown product. The filter cake was then washed with DMF and EtOH. The product was dried overnight in a vacuum oven at 60 °C.

2.2.2 Synthesis of the NMFA composites. The NMFA composites were obtained using the chemical precipitation method by controlling the mass proportions of NH$_2$-MIL-53(Fe) *versus* AgSCN. Firstly, 0.2 g of NH$_2$-MIL-53(Fe) was dispersed in 40 mL of the mixed solution and ultrasound was applied for 15 min. Then, a certain amount of NaSCN (0.1 M) solution was added into the mixed solution at the specific ratio. Subsequently, the suspension was transferred to a magnetic stirrer and stirred vigorously for 1 h. After that, the corresponding proportion of the AgNO$_3$ (1 M) solution was dropped slowly into the suspension, and the mixed solution was stirred for 24 h in the dark. Finally, after being filtered and washed, the composite sample was vacuum dried overnight at 60 °C, and the composites materials were designated as NMFA-*X*, *X* = 3, 4, 5, 6, corresponding to the amount of added AgSCN of 30, 40, 50, and 60 wt%. The preparation process is shown in Fig. 1.

2.3 Characterization of the as-prepared composites

The morphology of the composite material was analyzed using FESEM (ZEISS GeminiSEM 500, Germany) and HRTEM
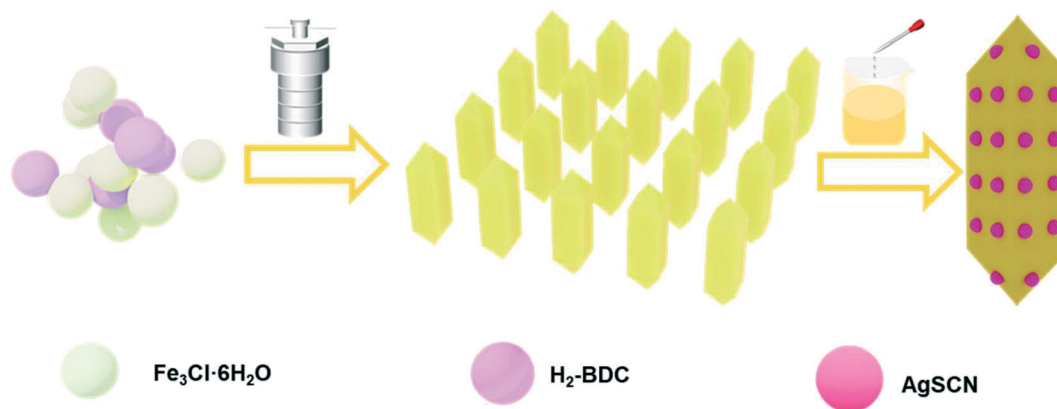
This journal is © The Royal Society of Chemistry 2022

React. Chem. Eng., 2022, **7**, 84–100 | 85

Fig. 1 Schematic illustration of the process for preparing the NH_2-MIL-53(Fe)/AgSCN composites.

(TecnaiG2 F20 S-TWIN, FEI, USA). The elemental mapping of NMFA-5 was carried out based on the FESEM characterization. The functional groups of the as-prepared simples were analyzed using Fourier transform infrared spectroscopy (FT-IR, NICOLET 5700, USA). The crystal structures were recorded using X-ray diffractometry (XRD, Bruker D8 Advance, Germany), and the scanning angle range was 5 to 60°. The ultraviolet-visible diffuse reflectance spectroscopy (DRS) spectrum of the as-prepared sample was obtained on a UV-vis spectrophotometer (U-3900, Japan). The binding energies of the elements in NH_2-MIL-53(Fe), AgSCN and NMFA-5 were performed using X-ray photoelectron spectroscopy (XPS, Escalab 250XI, Thermo Fisher, USA). The surface areas of the as-prepared sample were obtained using Brunauer–Emmett–Teller (BET) analysis (Quantachrome autosorb-iQ-2MP). The PL spectra with excitation wavelengths
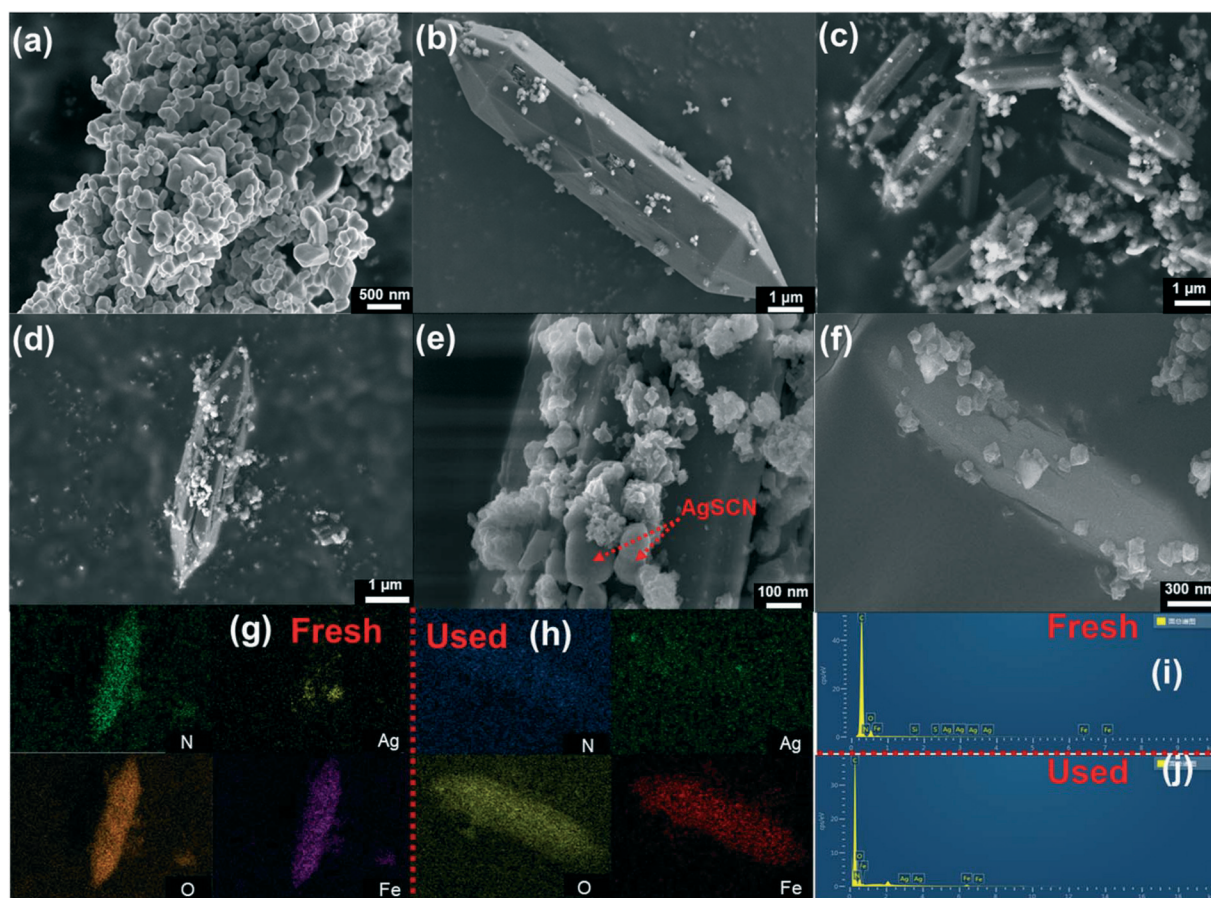

Fig. 2 SEM images of (a) AgSCN, (b) NH_2-MIL-53(Fe), (c)–(e) NMFA-5 and (f) NMFA-5 after H_2 production, element mapping results (g) and (h), and EDX spectra (i) and (j) of fresh NMFA-5 and after H_2 production.
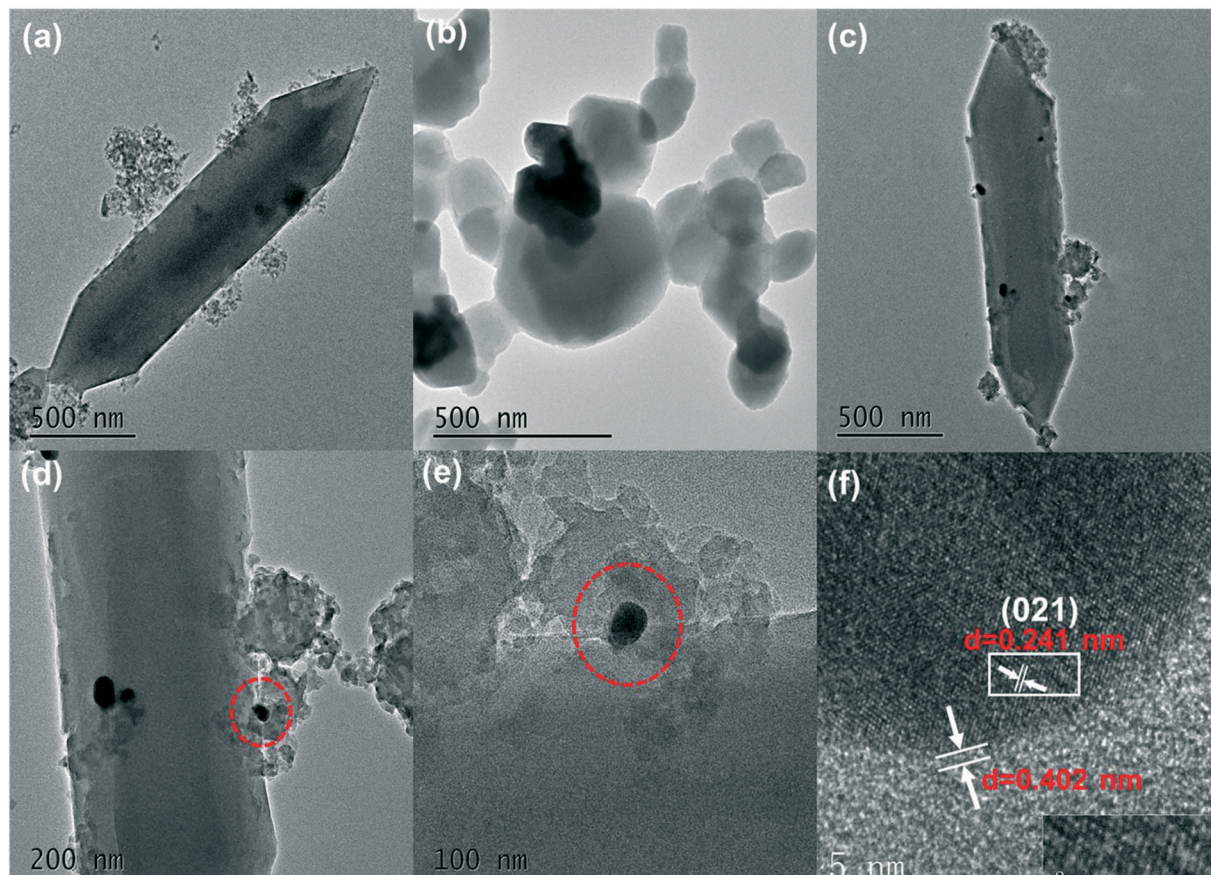
Fig. 3 TEM images of (a) NH$_2$-MIL-53(Fe) and (b) AgSCN; and HRTEM images of (c–f) NMFA-5.

of 375 nm were analyzed using a fluorescence spectrometer (F-4600 FL, Japan). The photocurrent, EIS and Mott–Schottky analysis were performed on a CHI 600 electrochemical workstation (Shanghai, China). The light source used was a 300 W xenon lamp (PLS-SXE 300).

2.4 Photocatalytic degradation of CIP and RhB

In this study, the photocatalytic activity was recorded by degradation of the CIP and RhB in solution and a 300 W Xe lamp ($\lambda > 420$ nm) was used. Specifically, 20 mg of the catalysts and 100 μL of H$_2$O$_2$ (30%, V/V%) were added into an aqueous solution of CIP or RhB aqueous solution (200 ml, 10%, V/V%) and stirred for 60 min in the dark. Then, 3 mL of the reaction solution was extracted every 10 min for analysis. The solid residues were removed using high speed centrifugation before testing. The concentration of CIP was analyzed *via* a PerkinElmer Lambda 35 spectrophotometer at 272 nm, and the inspection wavelength for RhB was set as 554 nm.

In addition, the highly efficient hydrogenation (HER) was performed in a 150 mL quartz reactor, in which 20 mg of the catalysts and quantitative EY and TEOA were added in 100 mL of aqueous solution. The solution was then kept under an uninterrupted vacuum for 30 min to remove the dissolved gas in the water. Before the reaction began, the gas

chromatography collecting system was purged with nitrogen. During the reaction period, the total H$_2$ production was analyzed every 30 min, and the HER system was run for 4 h to capture the full reaction.

3 Results and discussion

3.1 Characterization

The microstructures of the samples were observed by FESEM and TEM and the images are shown in Fig. 2 and 3. The microstructures of the AgSCN were observed to be spherical from Fig. 2a and 3a.[27] NH$_2$-MIL-53(Fe) appeared to be spindle-shaped and was surrounded by irregular debris (Fig. 2b and 3b), which could be attributed to the incomplete growth process.[28] As shown in Fig. 2c–e and 3c and d, the FESEM and HRTEM images of the NMFA-5 composite indicate that the AgSCN nanoparticles were anchored on the surface of NH$_2$-MIL53(Fe). The element mapping (Fig. 2g) and HRTEM images (Fig. 3c and d) of the NMFA-5 composite clearly show that the interface contact was formed between the spindle-shaped NH$_2$-MIL53(Fe) and AgSCN nanoparticles, which is beneficial for the transmission of electrons. The results of the element mapping and EDX characterization both proved the existence of AgSCN nanoparticles on the surfaces of the NH$_2$-MIL53(Fe), which also demonstrated that the NMFA composites were successfully synthesized. In
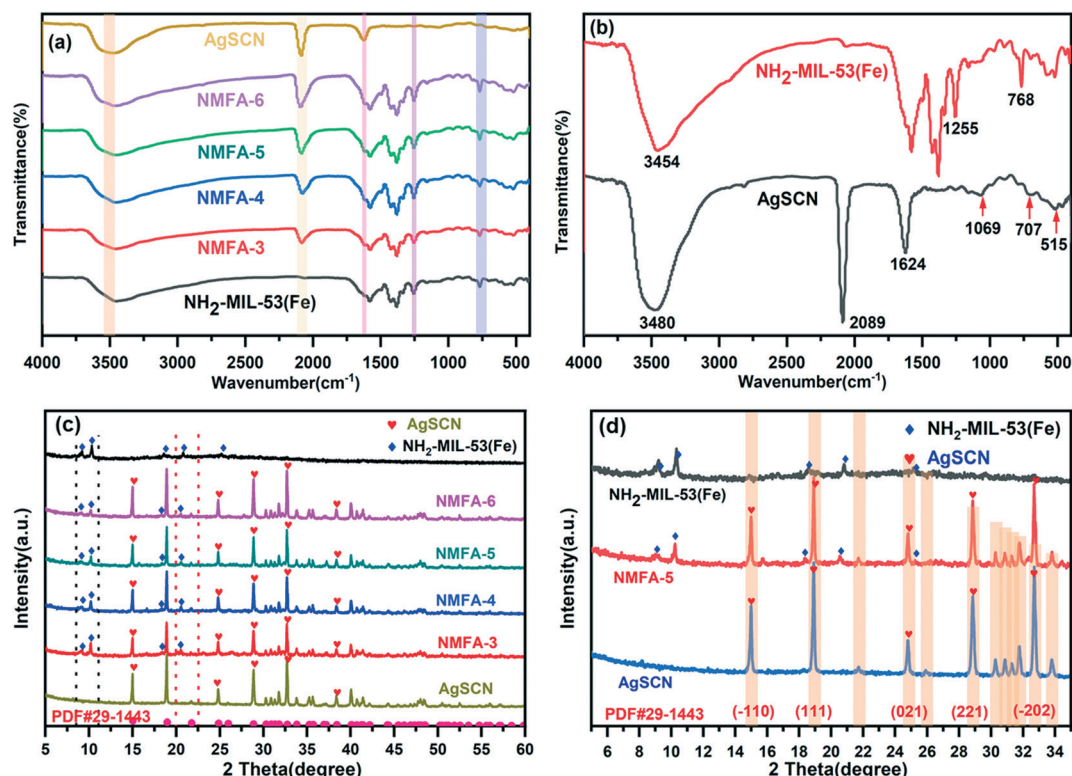
Fig. 4 (a) and (b) FT-IR spectra of the as-prepared samples; and (c) and (d) XRD patterns of the as-prepared samples.

addition, as shown in the SEM (Fig. 2f), element mapping (Fig. 2h), and EDX (Fig. 2j) images of the NMFA-5 composite after H_2 production, it was observed that the morphology of NH_2-MIL-53(Fe) did not show any significant changes after the reaction. In addition, the element mapping and EDX characterization also show that the AgSCN nanoparticles still exist on the surfaces of the NMFA-5 composite after the reaction. Furthermore, as shown in Fig. 3e for the NMFA-5 composite, the interplant spacing of AgSCN was 0.241 nm, which represented the (021) planes of the AgSCN. The connection pitch of the composites was 0.402 nm, which indicated that the composites were successfully synthesized.

The characteristic functional groups and crystal type information of the as-prepared NH_2-MIL-53(Fe) and NMFA composites was identified using FT-IR and XRD characterization. As shown in Fig. 4a, the NMFA composites contained both the characteristics of AgSCN and NH_2-MIL-53(Fe). Specifically, the vibrational bands located at 505, 707, 1069, and 2089 cm^{-1} represented the bending, symmetric stretching, bending overtones and asymmetric stretching vibrations of the SCN^{-1} group,[29] respectively. More precisely, the characteristic vibrational bands of 707 and 2089 cm^{-1} could be attributed to the S–C and C–N groups.[30,31] At the same time, the broad peak at 3450 cm^{-1} for all of the prepared samples could be attributed to the v(OH) stretching, and the weak band at 1620 cm^{-1} indicated that the composite existed in the AgSCN structure. The bands at 521, 768, 1255 and 3454 cm^{-1} were attributed to the Fe–O, C–H vibration of

the benzene rings, and the C–N and N–H vibrations of the amino group, respectively.[32,33] In short, the characteristic vibrational bands of the NMFA composites were very similar to those of the SCN^{-1} functional group, for which the bands were close to 770 and 2000 cm^{-1}. This conclusion proved that the NMFA composites were successfully synthesized. Notably, the vibrational band of the C–N functional group of AgSCN could overlap with the C–H vibrational band of the benzene ring of NH_2-MIL-53(Fe), which might lead to only one absorption peak being observed. XRD patterns of the as-prepared samples are shown in Fig. 4c. From the figure, it can easily be seen that the crystallographic features of NH_2-MIL-53(Fe) and AgSCN were consistent with those reported previously.[34] Specifically, the characteristic peaks at 9.2, 10.4, 13.1, 18.6, 20.8, and 25.1° were well matched with the standard in the card library for the Fe-MOFs, indicating that the NH_2-MIL-53(Fe) was successful synthesized. Otherwise, the four strong peaks at 15.0, 18.9, 28.9, and 32.8° of the AgSCN composite also matched well with the standard in the card library (PDF #29-1443), which could be indexed to the lattice plane of (−110), (111), (−202), and (221). The diffraction peaks of the NMFA composites were well-matched with the corresponding pure samples, which not only show that the structure was not changed during the synthesis process, but also further proved that the composites were successfully prepared. Furthermore, it can be observed that the characteristic peak of NH_2-MIL-53(Fe) became much weaker following the increase in the proportion of AgSCN in

88 | *React. Chem. Eng.*, 2022, **7**, 84–100

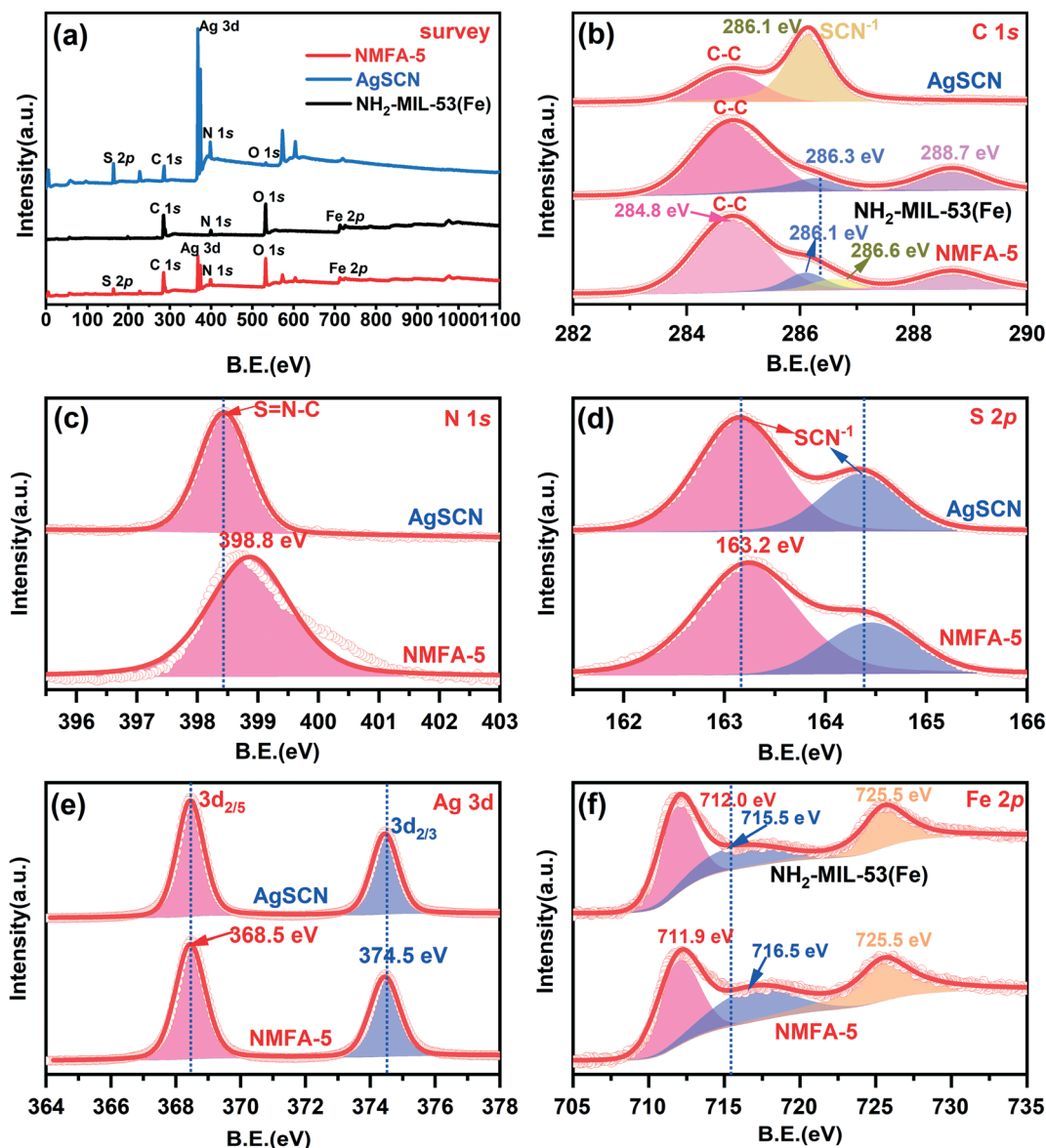This journal is © The Royal Society of Chemistry 2022

Fig. 5 XPS spectra of (a) the survey scan, and (b) C 1s, (c) N 1s, (d) S 2p, (e) Ag 3d, and (f) Fe 2p for the samples.

the NMFA-*x* compounds. Whereas the characteristic peak of AgSCN became much more obvious in contrast.

XPS measurements were used to reveal the chemical composition of the samples, and the results are displayed in Fig. 5. The full spectrum shows that NMFA-5 consisted of C, N, O, S, Fe, and Ag elements. Fig. 5b shows the C 1s spectrum of the NMFA-5 composite, the four peaks at 284.8, 286.1, 286.6 and 288.4 eV can be attributed to the C–C, C–O, SCN^{-1} and C–C≡N groups,[26] respectively. This indicates that the NMFA composites were successfully synthesized, and the subtle difference in the C–O group can be attributed to the SCN$^-$ groups. As shown in Fig. 5b in the N 1s spectrum of the NMFA-5 composite, there was only one peak located at 398.8 eV. Fig. 5d shows the S 2p spectrum of the composites, from which the two peaks at 163.2 and 164.4 eV can be easily found. The N 1s and S 2p characteristic peaks were both

attributed to the SCN$^-$ group of the NMFA-5 composite. However, it is worth noting that the N 1s peak shows a greater difference, while the S 2p does not. This indicates that the S element may play a major role in the SCN$^-$ group. As shown in Fig. 5e, the two peaks at 368.5 and 374.5 eV could be attributed to the 3d$_{2/5}$ and 3d$_{2/3}$ states of Ag$^+$.[25] Finally, as shown in Fig. 5f in the spectrum of Fe 2p, the two characteristic peaks at 712.0 and 725.5 eV correspond to Fe 2p$_{3/2}$ and Fe 2p$_{1/2}$. Meanwhile, there was a satellite signal located at 715.5 eV, which suggested that the Fe exists as a positive trivalent state.[35] However, the satellite signal peak of the NMFA-5 composites was centered at 716.5 eV, which was higher in energy than that of the pure NH$_2$-MIL-53(Fe). In particular, it can be observed that the satellite signal of Fe 2p$_{3/2}$ shows a slight change in the peak offset intensity (from 1.1 to 1.0 eV). This negative shift can be attributed to the
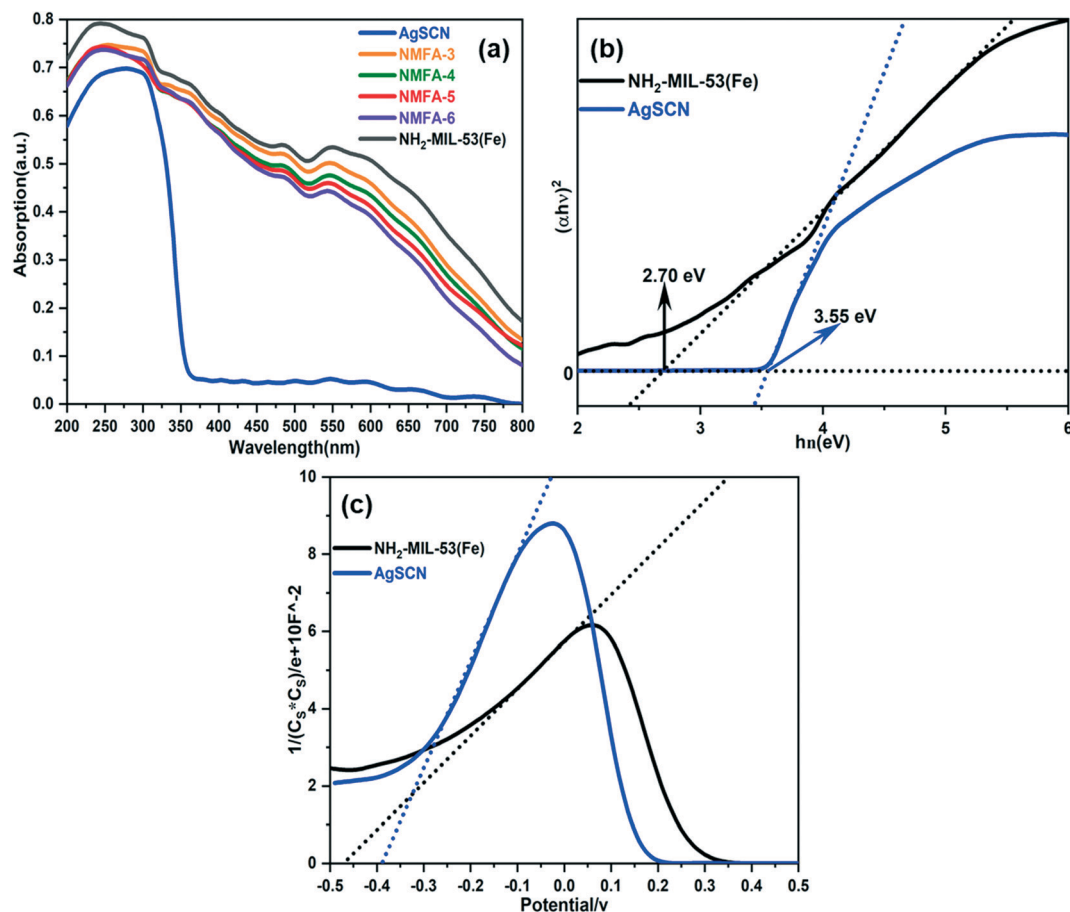
This journal is © The Royal Society of Chemistry 2022

React. Chem. Eng., 2022, **7**, 84–100 | **89**

Fig. 6 (a) UV-vis DRS spectra, (b) plots of $(\alpha h\nu)^2$ *versus* ($h\nu$) and (c) Mott–Schottky plots for the samples.

increased electron density of Fe^{3+}, and the binding energy of the peak representing Fe $2p_{1/2}$ shifts slightly (from 712.0 to 711.9 eV). Furthermore, this negative movement phenomenon indicates that the Fe^{3+} electron density is increased in the NMFA-5 composite. On the other hand, it is indicated that van der Waals forces (VDW) may exist between NH_2-MIL-53 (Fe) and AgSCN. In summary, the binding energies of the characteristic peaks for the C, N, and Ag elements of the NMFA-5 composites do not show much difference compared to those of the pure AgSCN, which can be attributed to the effect of the electronegativity of S in the SCN^- group. The binding energies of Fe^{3+} in the NMFA-5 composites became stronger, which could be caused by the effect of intimate contact between the surfaces of these two composites.

The optical adsorption performances of the synthesized samples were further measured using a UV-vis spectrophotometer and the spectra are shown in Fig. 6a. These results indicate that the NMFA composites exhibited a slightly weaker adsorption in the visible light region than in the pure light region. This indicates that the improvement of the photocatalytic performance might be significantly affected by some of the other aspects, such as the separation and transportation of the photo-generated electron–hole. Furthermore, the band-gap energy (E_g) was obtained using Tauc plots $((\alpha h\nu)^2 = A(h\nu - E_g))$.[36] As shown in Fig. 6b and c, the optical band gap of NH_2-MIL-53(Fe) and the AgSCN composites were calculated and found to be 2.70 and 3.55 eV. The conduction band (E_{CB}) potential of the catalysts was obtained from the Mott–Schottky plot (Fig. 6c). In addition, the valence band (E_{VB}) potential could be obtained using the formula $E_g = E_{VB} - E_{CB}$.[37] Detailed results are listed in Table 1.

Fig. 7 and Table 2 exhibit the surface area and pore structure parameters of the samples obtained using the BET method. The surface area of the samples follows the rule of NH_2-MIL-53(Fe) > NMFA-3 > NMFA-4 > NMFA-5 > NMFA-6 > AgSCN. The results showed that the introduction of AgSCN could increase the thickness of NH_2-MIL-53(Fe), thereby the average particle size of the NMFA composite increased while the specific surface area decreased. Furthermore, all the curves for the samples showed typical type IV isotherms and

Table 1 Calculated E_g, E_{VB} and E_{CB} potentials of the prepared samples based on the UV-vis results

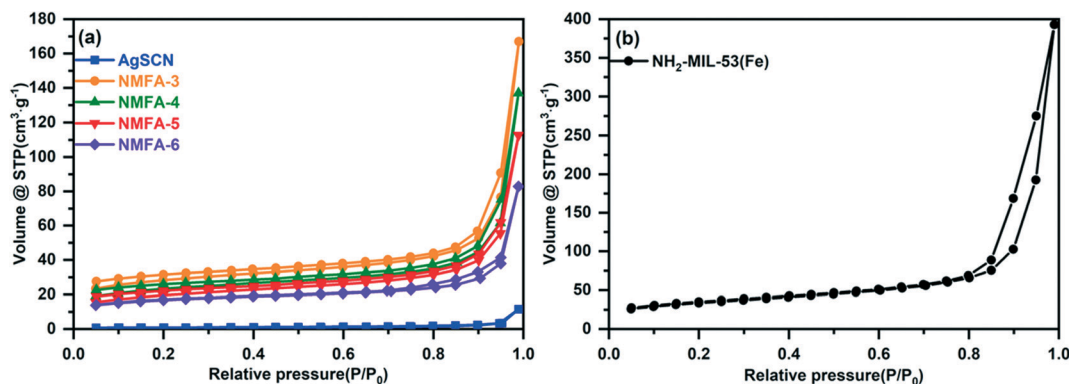| Sample serial number	E_g (eV)	E_{VB} potential (eV)	E_{CB} potential (eV)
NH_2-MIL-53(Fe)	2.70	2.23	−0.47
AgSCN	3.55	3.16	−0.39

Fig. 7 The N_2 adsorption–desorption isotherms for the (a) AgSCN and NMFA-x, (b) NH_2-MIL-53(Fe).

type H3 hysteresis rings, which could be attributed to the overlap between the composites.[38]

3.2 Photocatalytic activity

Fig. 8 shows that the photocatalytic activity of the NMFA-5 composites was the highest among the as-prepared catalysts. The degradation rate reached more than 90% for CIP within 60 min over the NMFA-5 composites, while for the pure NH_2-MIL-53(Fe) and AgSCN it only reached 50% and 27%. In addition, the degradation constants (k) of the NMFA-5, pure NH_2-MIL-53(Fe) and AgSCN were calculated as 0.03666, 0.00334, and 0.00088 min^{-1}, respectively (Fig. 8e). In the same way, the degradation rate reached almost 100% for RhB within 60 min over the NMFA-5 composites, while for the pure NH_2-MIL-53(Fe) and AgSCN the rates were just 55% and 49%. In addition, the degradation constants (k) of the NMFA-5, pure NH_2-MIL-53(Fe) and AgSCN were calculated as 0.09652, 0.00793, and 0.01044 min^{-1}, respectively (Fig. 8f). As NH_2-MIL-53(Fe) possesses a much larger surface area (119.569 m^2 g^{-1}) than the AgSCN (3.105 m^2 g^{-1}), which may be conducive to the high adsorption properties. Furthermore, the band gap of NH_2-MIL-53(Fe) was 2.70 eV, which should, in theory, show a good photocatalytic performance, while the results showed that the photocatalytic activity was not as high as expected. This may be related to the low separation and transfer efficiency of the photogenerated electrons and holes for the single NH_2-MIL-53(Fe). In sharp contrast, the NMFA composites all exhibited a much higher photocatalytic

performance than that of the pure samples, which could be attributed to the fact that the contact surface between NH_2-MIL-53(Fe) and AgSCN improved the separation and transport efficacy of the photogenerated electrons and holes. The detailed effects of NMFA on CIP and RhB photodegradation are shown in Table 3. In addition, Table 4 lists some of the typical photocatalysts used for the degradation of CIP or RhB that have been reported in recent years. Notably, although the dosage of the catalyst was significantly lower than the others, the photocatalytic activity of the NMFA composite was as high as that of the other novel photocatalysts. Furthermore, the photocatalytic performance of the NMFA composite was still maintained at a high level when the light source was restricted in the visible region. In light of these results, it can be concluded that the as-prepared NMFA composites exhibit competitive photocatalytic performances.

Furthermore, the photocatalytic stability is an important parameter that can be used to evaluate the catalysts from the perspective of practical applications. Cycling experiments were performed using the NMFA-5 composite for the degradation of CIP and RhB (Fig. 9a and b). The degradation rate of CIP and RhB for the NMFA-5 composite was maintained above 80% and 85% after five cycle experiments, respectively. The small decrease in the degradation rate can obviously be attributed to the inescapable leaching of the catalysts during the cycling experiments. Furthermore, there was no obvious difference displayed from the XRD pattern, which indicates the good stability of the as-prepared NMFA-5 composite (Fig. 9c). This could be attributed to the good protective effect of NH_2-MIL-53(Fe) with the introduction of AgSCN. Therefore, the NMFA composites exhibited a good structural and catalytic stability during the degradation.

Furthermore, the yield of H_2 evolution during the photocatalytic process under visible light radiation was also used to evaluate the photocatalytic performance of the as-prepared samples. The effect of the photosensitizer EY on the hydrogen production performance of the NMFA-5 composite is discussed first. As shown in Fig. 10a and b, the photocatalytic system with 30 mg EY showed the highest hydrogen production, the amount and rate of H_2 evolution were 298.09 μmol and 4742.43 μmol g^{-1} h^{-1}, respectively. This

Table 2 Detailed list of the surface area, pore volume and pore size of the samples

Sample	S_{BET} (m^2 g^{-1})	Average pore diameter (nm)	Pore volume (cm^3 g^{-1})	Average particle size (nm)
NH_2-MIL-53(Fe)	119.569	17.321	0.588	22.806
AgSCN	3.105	4.888	0.018	878.371
NMFA-3	103.861	3.852	0.219	26.259
NMFA-4	83.683	3.812	0.180	32.590
NMFA-5	69.457	3.806	0.147	39.266
NMFA-6	60.253	3.823	0.106	45.264

This journal is © The Royal Society of Chemistry 2022

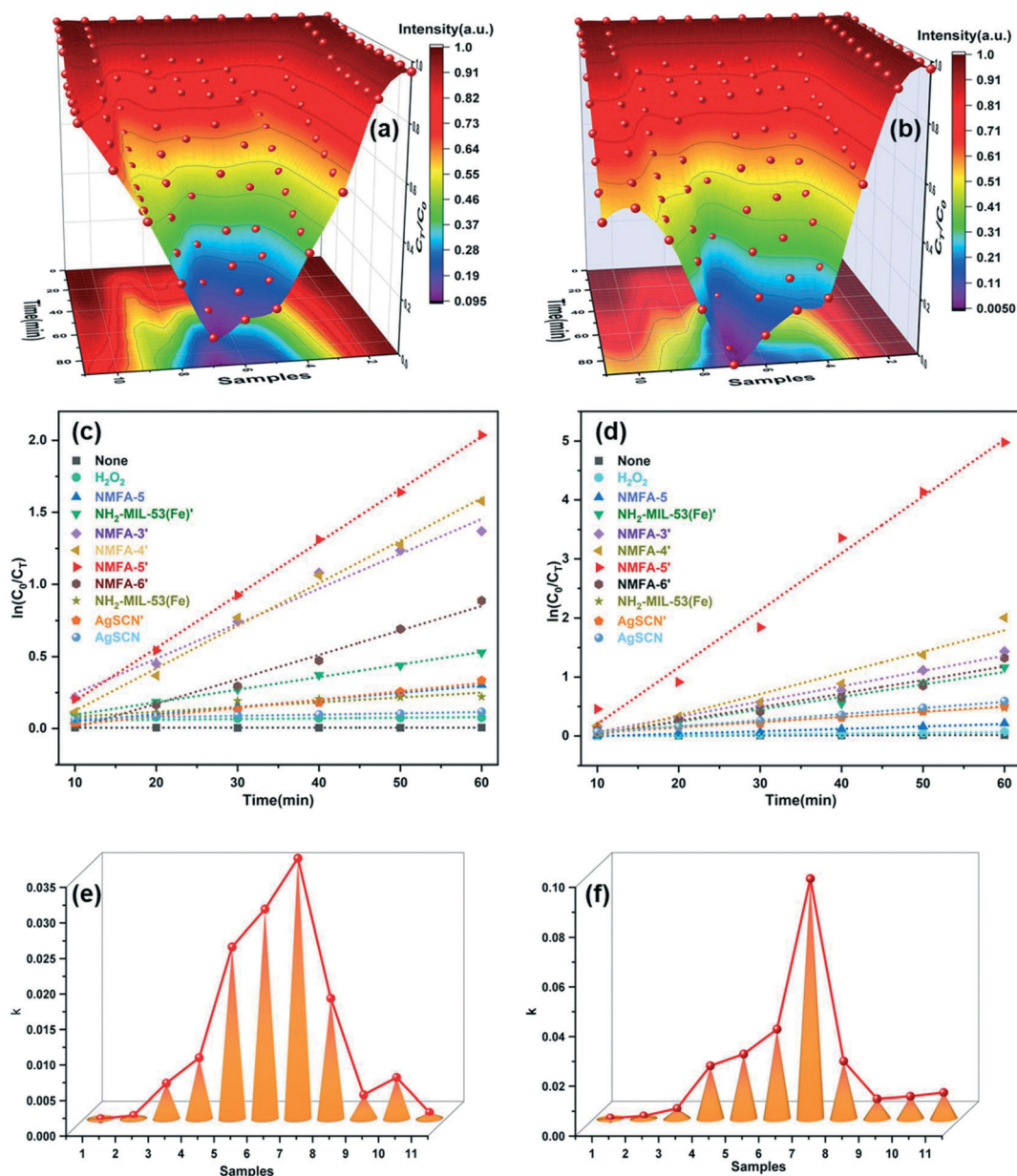React. Chem. Eng., 2022, 7, 84–100 | 91

Fig. 8 The photocatalytic performance of the samples for the degradation of CIP and RhB (a and b), the Pseudo-first-order kinetics curves (c and d) and the degradation constants k (e and f).

Table 3 Detailed list of the photocatalytic performances of the prepared samples

Sample	CIP (%)	RhB (%)	k (CIP)	k (RhB)
NH_2-MIL-53(Fe)(single)	49	56	0.00334	0.00793
NH_2-MIL-53(Fe)	63	78	0.00857	0.02120
AgSCN(single)	27	49	0.00088	0.01044
AgSCN	32	45	0.00678	0.00892
None	4	3	0.00006	0.00023
H_2O_2	12	9	0.00046	0.00110
NMFA-5(single)	43	40	0.00497	0.00411
NMFA-3	81	82	0.02420	0.02596
NMFA-4	84	90	0.02950	0.03599
NMFA-5	90	100	0.03666	0.09652
NMFA-6	71	80	0.01695	0.02310

result indicates that the amount and rate of hydrogen generated at different EY concentrations initially increased in the early stage and then decreased. This phenomenon could be attributed to the shielding effect of the photosensitizer.[42] Furthermore, the effect of TEOA on the hydrogen production performance of the NMFA-5 composite was also discussed. As shown in Fig. 10c and d, the photocatalytic system with 10 mL of TEOA showed the highest hydrogen production performance, and the amount of H_2 evolved was 298.21 μmol. It is worth noting that the highest hydrogen production rate in the first 30 min was 6305.80 μmol g^{-1} h^{-1} when the content of TEOA was 5 mL, after that the rate decreases sharply. This phenomenon could be attributed to the contact area of the TEOA and the catalysts. As the reaction

92 | *React. Chem. Eng.*, 2022, **7**, 84–100

This journal is © The Royal Society of Chemistry 2022

Table 4 Comparison of the photocatalytic efficiency of the NMFA composites and relevant catalysts reported in recent years

Samples	Amount of catalyst (g L^{-1})	Pollutants (ppm)	Xenon lamp (W)	Degradation rate (%)	Ref.
AgSCN	3	10, RhB	300 (<420 nm)	93.2	39
Bi$_2$O$_3$-TiO$_2$/PAC	1	20, CIP	300 (<420 nm)	96.9	40
NH$_2$-MIL-53(Fe)	0.25	10, RhB	500 (>420 nm)	86.16	41
NMFA-5	0.1	10, CIP	300 (>420 nm)	90.0	—
NMFA-5	0.1	10, RhB	300 (>420 nm)	100	—

progresses, the contact surface cannot be replenished and leads to a sharp decrease in the hydrogen production rate when the TEOA concentration is low. In addition, the NMFA-5 composite was repeatedly measured under the optimal conditions (the system contains 30 mg of EY and 10 mL of TEOA). As shown in Fig. 11a–c, the NMFA-5 composite showed a stable performance for the photocatalytic cracking of water to produce H$_2$. Fig. 11d–f shows the time course and rate of hydrogen generation for the NH$_2$-MIL-53(Fe), AgSCN and NMFA-x photocatalysts. The NMFA composites showed an obviously higher activity for photocatalytic hydrogen generation and the amounts of hydrogen produced were 142.48, 242.58, 298.21, and 244.18 μmol, respectively. The amount of hydrogen produced using NMFA-x was 1.97, 3.36, 3.13, 3.38, 6.52, 11.11, 13.65, and 11.18 times higher than that produced using NH$_2$-MIL-53(Fe) and AgSCN, respectively. At the same time, the

amount of H$_2$ evolution was only 72.26 and 21.84 μmol for the pure samples. This may be due to the lower transfer efficiency of the photogenerated electrons and holes. Furthermore, the high recombination rate of the electron–hole pairs may not be conducive to the reduction of H$^+$ in water by the photogenerated electrons to generate H$_2$.[43]

3.3 Charge separation efficiency and radical capture

In order to verify the mechanism of the enhanced photocatalytic performance for the NMFA composites, the spectra for the separation, migration and recombination of the photogenerated electron–hole pairs in the NMFA composites were studied. Firstly, the transient photocurrent response spectrum was used to analyze the separation efficiency of the electrons and holes. As shown in Fig. 12a, the NMFA-5 composite showed obviously enhanced
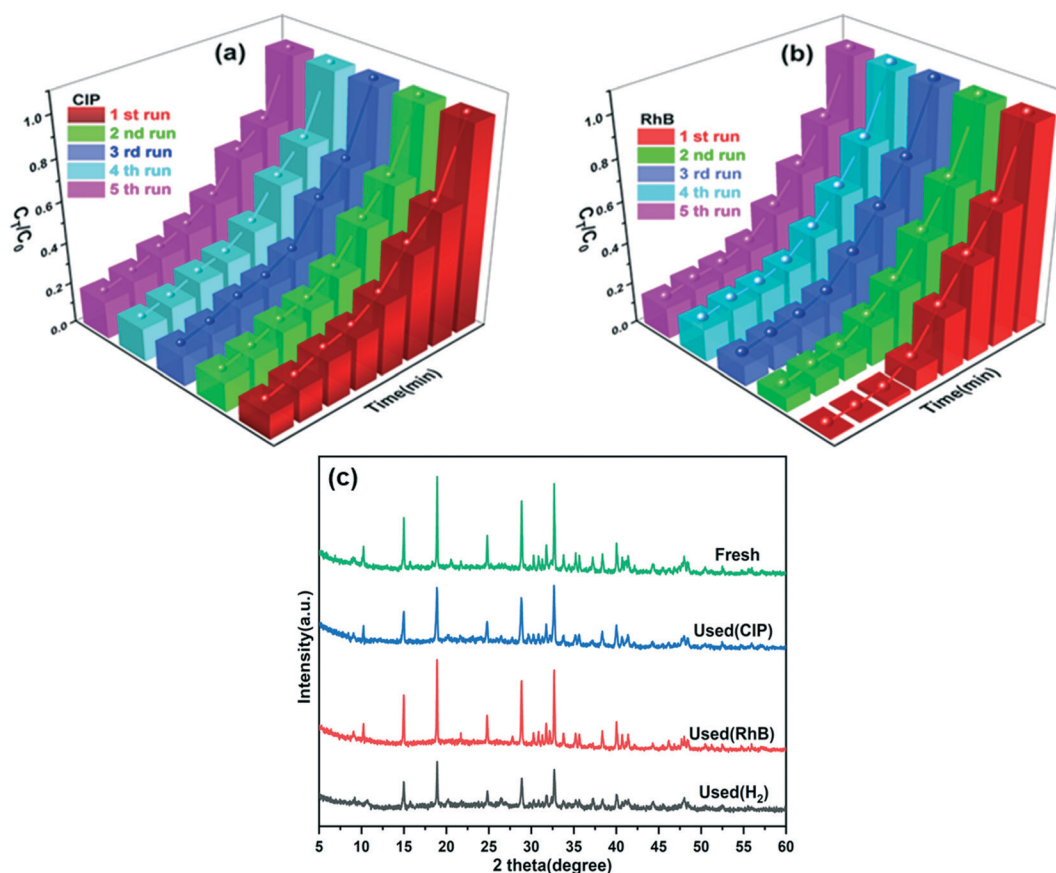
Fig. 9 (a and b) Catalytic cycle test results and (c) the XRD patterns of the NMFA-5 sample before and after the cycling test.
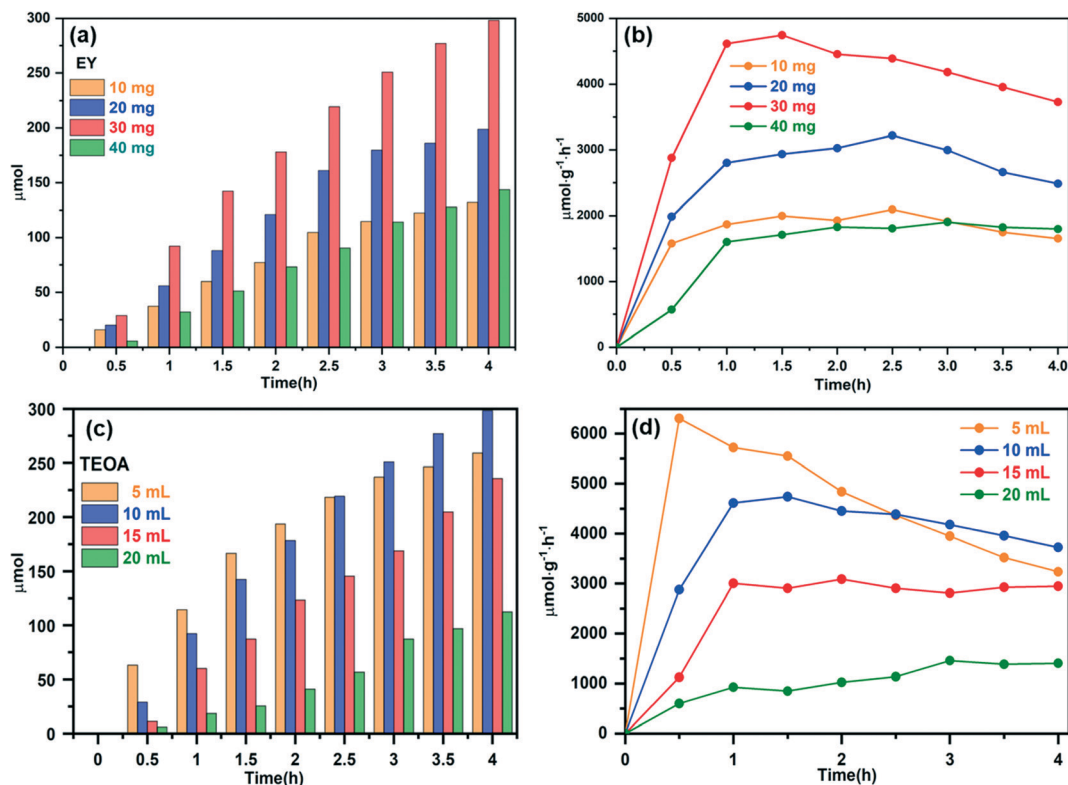
This journal is © The Royal Society of Chemistry 2022

React. Chem. Eng., 2022, **7**, 84–100 | **93**

Fig. 10 The effect of the photosensitizer EY (a) and (b) and TEOA (c) and (d) on the H$_2$ production performance.

photocurrent intensities compared to those of the pure samples. Similarly, the transfer efficiency of the photogenerated charges for the as-prepared composites was analyzed using EIS and Nyquist plots. As shown in Fig. 12b, the NMFA-5 composite obviously exhibited the smallest sized radius arc compared to those of the pure samples. The results indicated that the rapid movement of photogenerated carriers through close contact between NH$_2$-MIL-53(Fe) and AgSCN was more effective. Furthermore, the PL emission intensity reflected the separation effect of the photo-
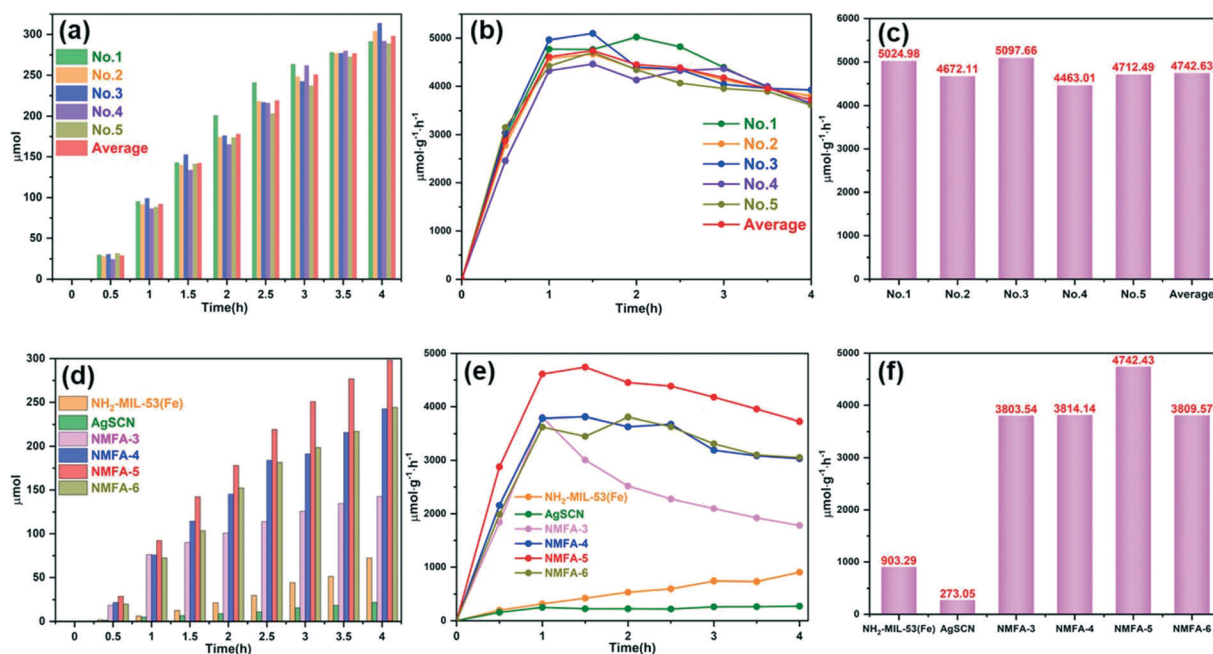

Fig. 11 The H$_2$ evolution performances of the NMFA-5 composites for five cycles (a)–(c), and different samples (d)–(f) under the same reaction conditions.

94 | *React. Chem. Eng.*, 2022, **7**, 84–100

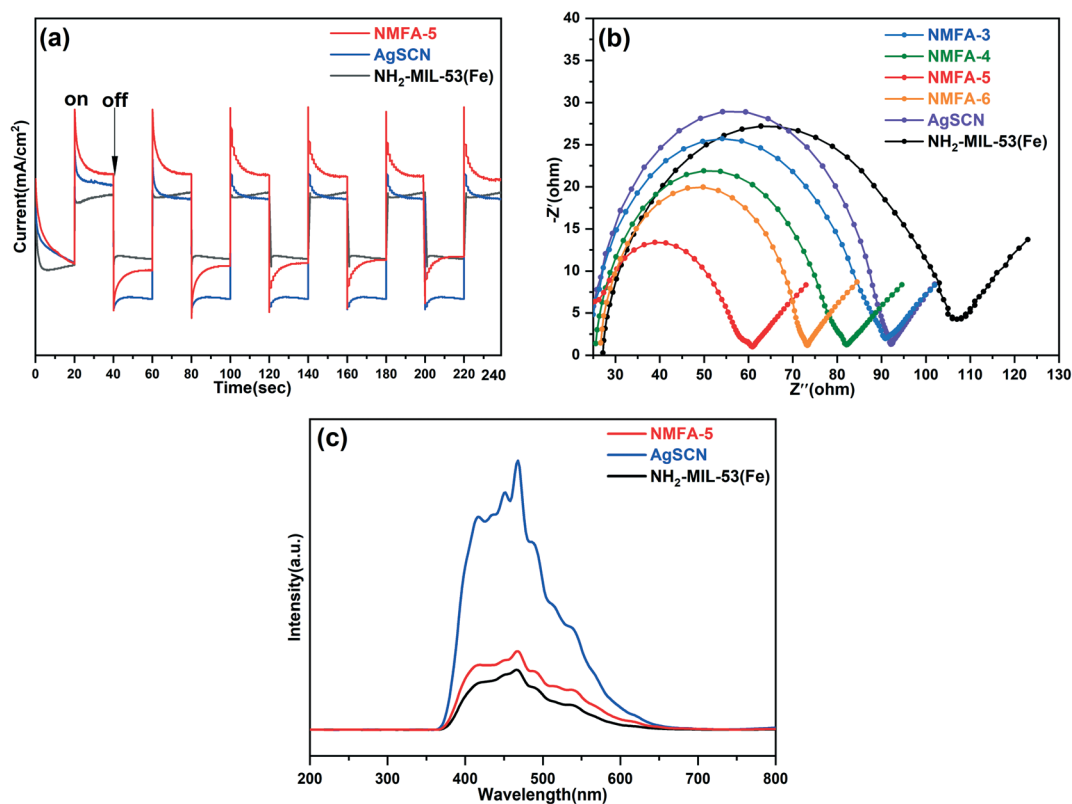This journal is © The Royal Society of Chemistry 2022

Fig. 12 Spectra showing the instantaneous photocurrent (a), EIS (b), and PL (c) of the samples.
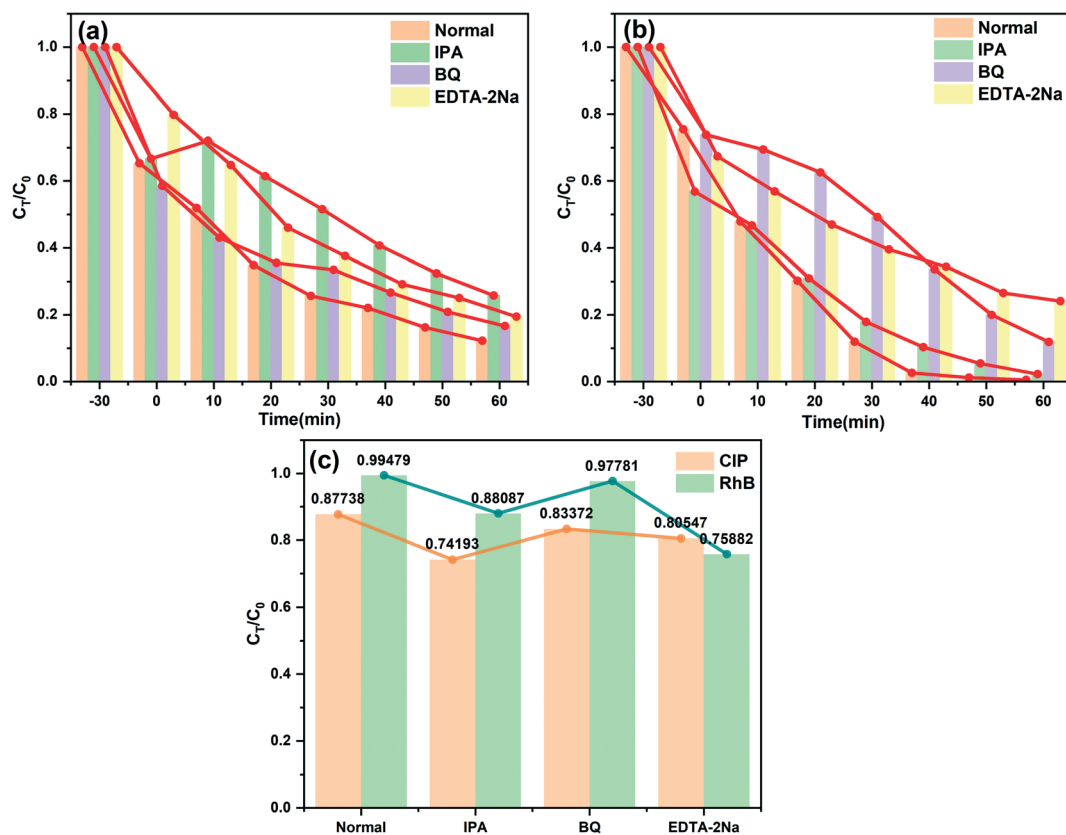

Fig. 13 The radical quenching results of the NMFA-5 composite for the degradation process of the CIP (a) and RhB (b), and the results comparison (c).
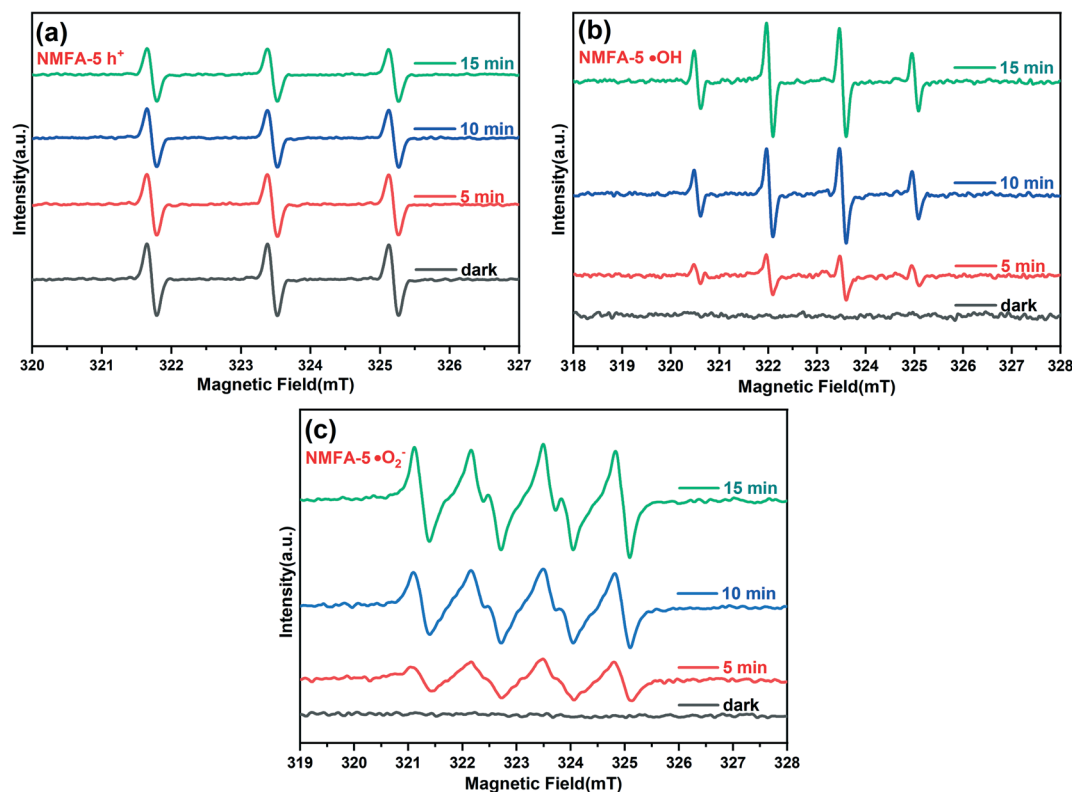
This journal is © The Royal Society of Chemistry 2022

React. Chem. Eng., 2022, 7, 84–100 | 95

Fig. 14 The ESR spectra of (a) h^+, (b) $\cdot OH$ and (c) $\cdot O_2^-$ generated using the NMFA-5 composites.

generated charge. As shown in Fig. 12c, the peak for the NMFA-5 composite was much lower than that of the pure samples. The results indicated that the close contact between NH_2-MIL-53(Fe) and AgSCN could enhance the separation efficiency of the photogenerated electrons and holes.

Generally, the photocatalytic mechanism is studied using active species trapping experiments. The hydroxyl radicals ($\cdot OH$), superoxide radicals ($\cdot O_2^-$) and holes (h^+) were eliminated using IPA (1 mmol), BQ (benzoquinone, 1 mmol), and EDTA-2Na (1 mmol) during the photocatalytic removal of pollutants in wastewater, respectively. The quencher was dissolved in wastewater before the adsorption and desorption equilibrium was reached. As shown in the experimental results shown in Fig. 13, it is indicated that the photocatalytic performance of the NMFA-5 composites was significantly inhibited compared with the results obtained without the addition of an elimination agent. From the experimental results, it can be easily observed that the greatest inhibitory effect was found upon adding IPA during CIP degradation. This indicated that the $\cdot OH$ occupies an important position in the CIP degradation process. Correspondingly, the h^+ played a more prominent role than the $\cdot OH$ radicals in the RhB degradation process, which might be attributed to the characteristics of different pollutants. In addition, the superoxide radicals ($\cdot O_2^-$) only provided a small contribution to the degradation of CIP and RhB, indicating that $\cdot O_2^-$ played a small role in the reaction.

To further understand the influence of the h^+ and $\cdot OH$ radicals in the photocatalytic process, ESR measurement was performed for the NMFA-5 composite. During the ESR measurement, the free radical signals were recorded in the same period of time at room temperature under xenon lamp radiation. Specifically, about 20 mg of the samples were added into the solution containing 50 mM of the spin trapped reagents, which were 5,5-dimethyl-1-pyrroline N-oxide (DMPO)/H_2O, methanol/DMPO and 2,2,6,6-tetramethyl-piperidinooxy (TEMPO)/chlorpromazine hydrochloride for the trapping of the radicals $\cdot OH$, $\cdot O_2^-$, and h^+, respectively. As shown in Fig. 14a, the three strong characteristic peaks belonging to the h^+ decreased as the illumination time increased, which indicated that the h^+ radical participated in the process of degradation. As shown in Fig. 14a, the peak intensity of the four characteristic peaks increased with the increased irradiation time, which indicated that the h^+ radical participated in the process of degradation. Furthermore, as shown in Fig. 14b, four characteristic peaks for $\cdot OH$ were detected after the light was switched on. In addition, the peak intensity increased with the prolonged irradiation time, which indicated the existence of the $\cdot OH$ radical during the process of degradation. In addition, as shown in Fig. 14c, the peak intensity of the six characteristic peaks also increased with the prolonged irradiation time. The results indicated that the $\cdot O_2^-$ radicals were also produced during the photocatalytic degradation process. The oxidation potential of the free radicals was proportional to the oxidation capacity in the optical Fenton
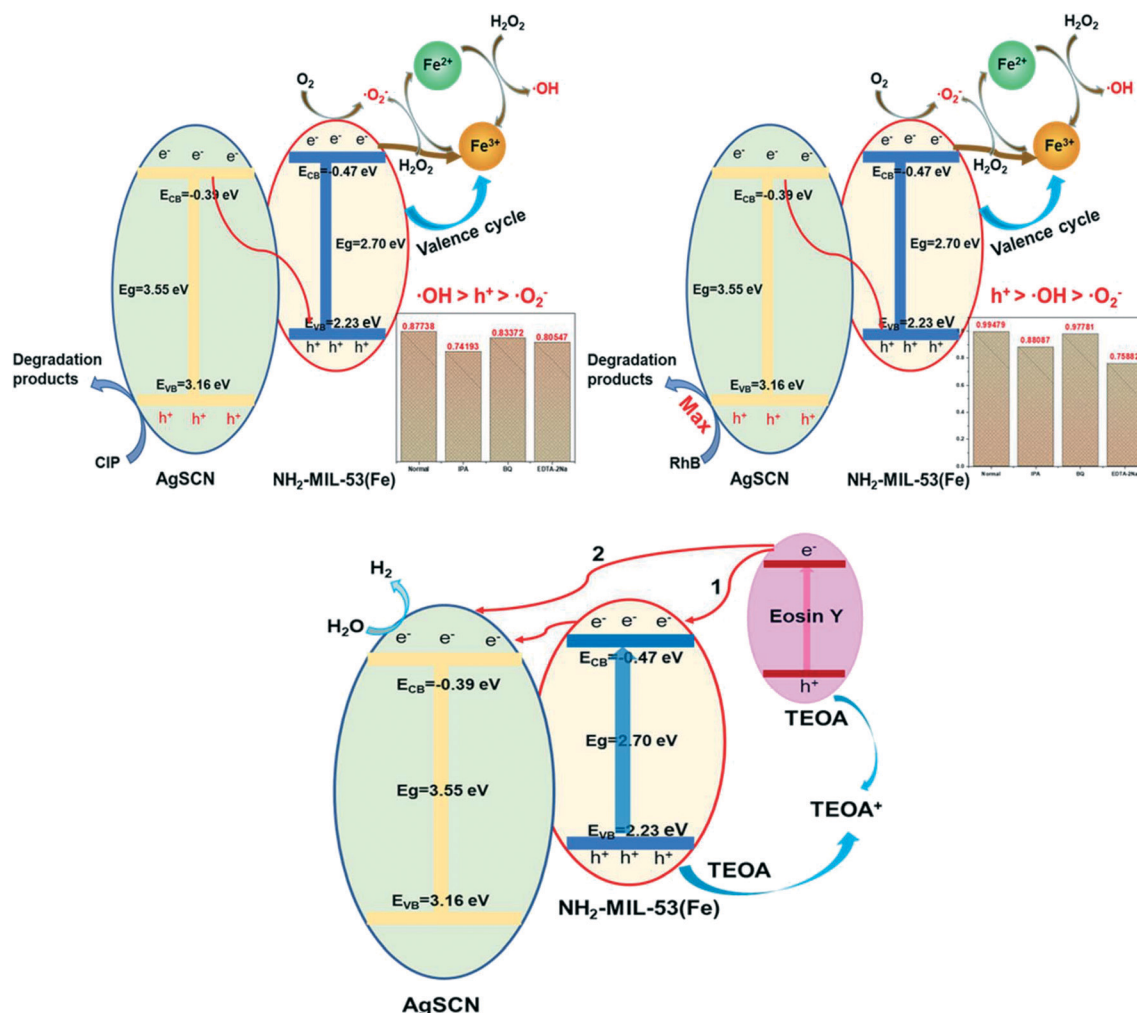
Fig. 15 Proposed schematic diagram of the possible charge transfer approach of the NMFA composite for the degradation of pollutants and hydrogen production.

system. In particular, the oxidation potentials for the OH$^{\cdot}$ and $^{\cdot}O_2^-$ radicals were 2.73 and 1.3 eV, respectively. As expected, the $^{\cdot}OH$ radicals were obtained before the $^{\cdot}O_2^-$ radicals in the optical Fenton system. Therefore, the $^{\cdot}O_2^-$ radicals played a small role in the contaminant photo-degradation process.

3.4 Mechanism of photocatalysis

UV-vis DRS and Mott–Schottky characterizations are considered, in theory, to be the most effective means to explore the photocatalytic mechanism of the composites. As shown in Fig. 7, the E_g of NH_2-MIL-53(Fe) and AgSCN were calculated as 2.70 and 3.55 eV, and the E_{CB} values were found to be −0.47 and −0.39 eV, respectively. Therefore, the E_{VB} of NH_2-MIL-53(Fe) and AgSCN were +2.23 and +3.16 eV according to the formula $E_g = E_{VB} - E_{CB}$. As shown in Fig. 15, when the NMFA-5 composites were irradiated using visible light, the photogenerated electrons were excited on the surfaces of the NH_2-MIL-53(Fe) and participated in the reduction of Fe^{3+}. At the same time, the electrons on the

conduction band (CB) of AgSCN undergo directional migration to the valence band (VB) of NH_2-MIL-53(Fe) owing to the large number of h$^+$ that accumulate on the VB of NH_2-MIL-53(Fe). In addition, the h$^+$ could take part in the degradation of the pollutants, which originates from that remaining in the VB of AgSCN. At the same time, the mutual conversion between Fe^{3+} and Fe^{2+} in the optical Fenton system could generate free radicals for the degradation of pollutants molecules. However, the free radicals h$^+$, $^{\cdot}OH$, $^{\cdot}O_2^-$ played difference roles in the degradation of different pollutant molecules. This may be caused by the selectivity of the NMFA-5 photocatalyst to the pollutants with different characteristic groups. However, the mechanism for the visible-light photocatalytic H_2 evolution of the NMFA-5 photocatalyst was different from the photo-degradation reaction. Owing to the wide band gap of AgSCN ($E_g = 3.55$ eV) and the fact that EY and AgSCN were employed as the photosensitizer and co-catalyst during the photocatalytic reaction, respectively. The photogenerated electrons at a high potential on EY could migrate in the direction of a low potential if the system absorbs visible light (route 1). After

that, the electrons accumulated on the CB of NH_2-MIL-53(Fe) could migrate to the more negative CB of AgSCN. On the other hand, the electrons on the CB of EY could also directly migrate to the CB of AgSCN in one step (route 1). Finally, the high concentration of electrons accumulated on the CB of AgSCN could reduce the H^+ in the water to produce H_2. Furthermore, the h^+ in the VB of eosin Y and NH_2-MIL-53(Fe) reconverted to the ground state using the electron donor to maintain the balance of electrons and holes in the photocatalyst. This mechanism allowed H_2 production to proceed in an orderly manner.

4 Conclusion

In this research, highly active NMFA composites photocatalyst was successfully preparation through a chemical precipitation method. The prepared photocatalyst shows highly effective photocatalytic activity for CIP and RhB degradation, as well as excellent H_2 evolution efficacy. For the NMFA-5 composite, a degradation rate as higher as 90% and 100% was achieved for CIP and RhB degradation within 60 min. In particular, the degradation rate for the NMFA-5 composite was 1.8 and 1.82 times greater than that of the pure NH_2-MIL-53(Fe) and AgSCN samples for CIP degradation, and 3.3 and 2.08 times for the degradation of RhB. In addition, the highest H_2 production rate obtained for the NMFA-5 composites catalyst was 4742 μmol g^{-1} h^{-1}, which was 5.25 and 17.37 times greater than that of the pure samples. Optical characterization and a series of electrochemical characterization methods were used to analyze the composite microstructure and morphology. The PL, EIS and transient response current results jointly indicate that the composite material showed an excellent charge separation and transfer efficiency. In summary, the excellent photocatalytic performance of the NMFA-5 composites may provide potential solutions to environmental and energy issues.

Conflicts of interest

The authors declare that there is no conflict of interest regarding the publication of this paper.

Acknowledgements

References

1   H. Li, L. Zhang, H. Lu, J. Ma, X. Zhou, Z. Wang and C. Yi, Macro−/nanoporous Al-doped ZnO/cellulose composites based on tunable cellulose fiber sizes for enhancing photocatalytic properties, *Carbohydr. Polym.*, 2020, **250**, 116873.

2   B. Janani, K. M. Alarjani, L. L. Raju, A. M. Thomas, A. Das and S. S. Khan, A potent multifunctional Ag/Co-polyvinylpyrrolidone nanocomposite for enhanced detection of Cr(III) from environmental samples and its photocatalytic and antibacterial applications, *Spectrochim. Acta, Part A*, 2020, **243**, 118766.

3   L. Chen, X. Wang, Y. Chen, Z. Zhuang, F.-F. Chen, Y.-J. Zhu and Y. Yu, Recycling heavy metals from wastewater for photocatalytic CO_2 reduction, *Chem. Eng. J.*, 2020, **402**, 125922.

4   X. He, Z. Liu, Y. Yang, L. Li, L. Wang, A. Li, Z. Qu and F. Xu, Sensitivity Enhancement of Nucleic Acid Lateral Flow Assays through a Physical-Chemical Coupling Method: Dissoluble Saline Barriers, *ACS Sens.*, 2019, **4**, 1691–1700.

5   L. S. M. Nazir, Y. F. Yeong and T. L. Chew, Methods and synthesis parameters affecting the formation of FAU type zeolite membrane and its separation performance: a review, *J. Asian Ceram. Soc.*, 2020, **8**, 553–571.

6   Z. Zhou, Z. Shen, Z. Cheng, G. Zhang, M. Li, Y. Li, S. Zhan and J. C. Crittenden, Mechanistic insights for efficient inactivation of antibiotic resistance genes: a synergistic interfacial adsorption and photocatalytic-oxidation process, *Sci. Bull.*, 2020, **65**, 2107–2119.

7   Y. Zhen, Q. Zhang, X. Zhang, G. Zhang, X. Chen and C. Zhao, A novel tubular up-flow magnetic film photocatalytic system optimized by main factors control for efficient removal of chlorophenols wastewater, *J. Hazard. Mater.*, 2020, **398**, 122963.

8   L. Sun, S. Yin, D. Shen, Y. Zhou, J. Li, X. Li, H. Wang, P. Huo and Y. Yan, Fabricating acid-sensitive controlled PAA@Ag/AgCl/CN photocatalyst with reversible photocatalytic activity transformation, *J. Colloid Interface Sci.*, 2020, **580**, 753–767.

9   J. Zhang, Y. Guo, B. Shang, T. Fan, X. Lian, P. Huang, Y. Dong, Z. Chen and X. Yi, Unveiling the Synergistic Effect between Graphitic Carbon Nitride and Cu_2O toward CO_2 Electroreduction to C_2H_4, *ChemSusChem*, 2021, **14**, 929–937.

10 H. Huang, J. Zhao, Y. Du, C. Zhou, M. Zhang, Z. Wang, Y. Weng, J. Long, J. Hofkens, J. A. Steele and M. B. J. Roeffaers, Direct Z-Scheme Heterojunction of Semicoherent $FAPbBr_3$/Bi_2WO_6 Interface for Photoredox Reaction with Large Driving Force, *ACS Nano*, 2020, **14**, 16689–16697.

11 Y. Xu, J. Xu, W. Yan, H. Tang and G. Tang, Synergistic effect of a noble metal free MoS_2 co-catalyst and a ternary Bi_2S_3/MoS_2/P_{25} heterojunction for enhanced photocatalytic H_2 production, *Ceram. Int.*, 2021, **47**, 8895–8903.

12 D. Z. Zee, M. Nippe, A. E. King, C. J. Chang and J. R. Long, Tuning Second Coordination Sphere Interactions in Polypyridyl-Iron Complexes to Achieve Selective Electrocatalytic Reduction of Carbon Dioxide to Carbon Monoxide, *Inorg. Chem.*, 2020, **59**, 5206–5217.

13 X. Fang, S. Kalathil and E. Reisner, Semi-biological approaches to solar-to-chemical conversion, *Chem. Soc. Rev.*, 2020, **49**, 4926–4952.

14 H. Yang, H. Amari, L. Liu, C. Zhao, H. Gao, A. He, N. D. Browning, M. A. Little, R. S. Sprick and A. I. Cooper, Nano-assemblies of a soluble conjugated organic polymer and an inorganic semiconductor for sacrificial photocatalytic hydrogen production from water, *Nanoscale*, 2020, **12**, 24488–24494.

15 J. Cho, N. S. Suwandaratne, S. Razek, Y. H. Choi, L. F. J. Piper, D. F. Watson and S. Banerjee, Elucidating the Mechanistic Origins of Photocatalytic Hydrogen Evolution Mediated by MoS_2/CdS Quantum-Dot Heterostructures, *ACS Appl. Mater. Interfaces*, 2020, **12**, 43728–43740.

16 A. Fujishima and K. Honda, Electrochemical photocatalysis of water at semiconductor electrode, *Nature*, 1972, **238**, 37–38.

17 J. Sun, C. H. Shen, J. Guo, H. Guo, Y. F. Yin, X. J. Xu, Z. H. Fei, Z. T. Liu and X. J. Wen, Highly efficient activation of peroxymonosulfate by Co_3O_4/Bi_2WO_6 p-n heterojunction composites for the degradation of ciprofloxacin under visible light irradiation, *J. Colloid Interface Sci.*, 2021, **588**, 19–30.

18 L. Huang, D. Bao, X. Jiang, J. Li, L. Zhang and X. Sun, Fabrication of stable high-performance urchin-like CeO_2/ZnO@Au hierarchical heterojunction photocatalyst for water remediation, *J. Colloid Interface Sci.*, 2021, **588**, 713–724.

19 P. Chen, L. Chen, S. Ge, W. Zhang, M. Wu, P. Xing, T. B. Rotamond, H. Lin, Y. Wu and Y. He, Microwave heating preparation of phosphorus doped g-C_3N_4 and its enhanced performance for photocatalytic H_2 evolution in the help of Ag_3PO_4 nanoparticles, *Int. J. Hydrogen Energy*, 2020, **45**, 14354–14367.

20 X. Dai, L. Chen, Z. Li, X. Li, J. Wang, X. Hu, L. Zhao, Y. Jia, S. X. Sun, Y. Wu and Y. He, CuS/$KTa_{0.75}Nb_{0.25}O_3$ nanocomposite utilizing solar and mechanical energy for catalytic N_2 fixation, *J. Colloid Interface Sci.*, 2021, **603**, 220–232.

21 L. Chen, X. Dai, X. Li, J. Wang, H. Chen, X. Hu, H. Lin, Y. He, Y. Wu and M. Fan, A novel Bi_2S_3/$KTa_{0.75}Nb_{0.25}O_3$ nanocomposite with high efficiency photocatalytic and piezocatalytic N_2 fixation, *J. Mater. Chem. A*, 2021, **9**, 13344–13354.

22 Y. S. Wei, M. Zhang, R. Zou and Q. Xu, Metal-Organic Framework-Based Catalysts with Single Metal Sites, *Chem. Rev.*, 2020, **120**, 12089–12174.

23 Y. Li, Y. Xia, K. Liu, K. Ye, Q. Wang, S. Zhang, Y. Huang and H. Liu, Constructing Fe-MOF-Derived Z-Scheme Photocatalysts with Enhanced Charge Transport: Nanointerface and Carbon Sheath Synergistic Effect, *ACS Appl. Mater. Interfaces*, 2020, **12**, 25494–25502.

24 X. Zhao, X. Yi, S. Tian and J. Zhang, Excellent photocatalytic degradation and disinfection performance of a novel bifunctional Ag@AgSCN nanostructure with exposed {−112} facets, *New J. Chem.*, 2018, **42**, 11811–11818.

25 J. Zhang, X. Liu, Q. Liu, Y. Licao, G. Liu and X. Shi, Z-scheme AgSCN/Ag_3PO_4/C_3N_4 heterojunction with excellent photocatalytic degradation of ibuprofen, *Ceram. Int.*, 2020, **46**, 106–113.

26 J. Song, M. Zhang, C. Yan, X. Zhao, G. Liu and J. Zhang, AgSCN/AgCl/FeOCl nanosheets heterojunction with novel interface structure and excellent photocatalytic performance, *J. Alloys Compd.*, 2020, **836**, 155544.

27 M. Yang and J. Ma, Synthesis and characterizations of AgSCN nanospheres using AgCl as the precursor, *Appl. Surf. Sci.*, 2009, **255**, 9323–9326.

28 S. M. Khoshfetrat, H. Khoshsafar, A. Afkhami, M. A. Mehrgardi and H. Bagheri, Enhanced Visual Wireless Electrochemiluminescence Immunosensing of Prostate-Specific Antigen Based on the Luminol Loaded into MIL-53(Fe)-NH_2 Accelerator and Hydrogen Evolution Reaction Mediation, *Anal. Chem.*, 2019, **91**, 6383–6390.

29 A. I. Ogarkov, A. S. Chernyavskii, S. G. Sakharov and K. A. Solntsev, Single-step incorporation of oh groups into the monosubstituted dodecahydro-closo-dodecaborate(2-) anion derivatives $[B_{12}H_{11}SCN]^{2-}$, $[B_{12}H_{11}I]^{2-}$, and $[B_{12}H_{11}OC(O)CH_3]^{2-}$, *Inorg. Mater.*, 2011, **47**, 1268–1270.

30 E. Diana, G. Gervasio, E. Priola and E. Bonometti, A new heterometallic multiligand 3D coordination polymer: synthesis and structure of $[Pb(OH)]_n[Ag(SCN)(CN)]_n$, *CrystEngComm*, 2014, **16**, 10040–10045.

31 X. Liu, P. Long, X. Wang, Z. Gao, Y. Lü and Z. Yi, Efficient Raman scattering response and large piezoelectricity in noncentrosymmetric $MnHg(SCN)_4$ crystals, *J. Mater. Chem. C*, 2017, **5**, 3238–3246.

32 Y. Tian, J. Song, Y. Zhu, H. Zhao, F. Muhammad, T. Ma, M. Chen and G. Zhu, Understanding the desulphurization process in an ionic porous aromatic framework, *Chem. Sci.*, 2019, **10**, 606–613.

33 Z. Yuan, X. Ma, X. Wu, G. Zhang, X. Wang, S. Wang and Y. Jia, Characterization of $Fe_5(AsO_3)_3Cl_2(OH)_{4.5}H_2O$, a new ferric arsenite hydroxychloride precipitated from $FeCl_3$-As_2O_3-HCl solutions relevant to arsenic immobilization, *J. Environ. Sci.*, 2020, **90**, 205–215.

34 F. Dai, Y. Wang, X. Zhou, R. Zhao, J. Han and L. Wang, $ZnIn_2S_4$ decorated Co-doped NH_2-MIL-53(Fe) nanocomposites for efficient photocatalytic hydrogen production, *Appl. Surf. Sci.*, 2020, **517**, 146161.

35 L. Shi, T. Wang, H. Zhang, K. Chang, X. Meng, H. Liu and J. Ye, An Amine-Functionalized Iron(III) Metal-Organic Framework as Efficient Visible-Light Photocatalyst for Cr(VI) Reduction, *Adv. Sci.*, 2015, **2**, 1500006.

36 A. Alshehri and K. Narasimharao, PtO_x-TiO_2 anatase nanomaterials for photocatalytic reformation of methanol to hydrogen: effect of TiO_2 morphology, *J. Mater. Res. Technol.*, 2020, **9**, 14907–14921.

37 A. Das, P. M. Kumar, M. Bhagavathiachari and R. G. Nair, Hierarchical ZnO-TiO_2 nanoheterojunction: A strategy driven approach to boost the photocatalytic performance through the synergy of improved surface area and interfacial charge transport, *Appl. Surf. Sci.*, 2020, **534**, 146161.

38 J. Yu, W. Xiong, X. Li, Z. Yang, J. Cao, M. Jia, R. Xu and Y. Zhang, Functionalized MIL-53(Fe) as efficient adsorbents for removal of tetracycline antibiotics from aqueous solution, *Microporous Mesoporous Mater.*, 2019, **290**, 109642.

39 S. Zhang, S. Zhang, L. Song, X. Wu and S. Fang, Synthesis and photocatalytic property of a new silver thiocyanate semiconductor, *Chem. Eng. J.*, 2014, **243**, 24–30.

This journal is © The Royal Society of Chemistry 2022

React. Chem. Eng., 2022, **7**, 84–100 | 99

40 X. Zhuang, X. Li, Y. Yang, N. Wang, Y. Shang, Z. Zhou, J. Li and H. Wang, Enhanced Sulfamerazine Removal via Adsorption–Photocatalysis Using Bi_2O_3–TiO_2/PAC Ternary Nanoparticles, *Water*, 2020, **12**, 2273.

41 Q. Zhao, L. Zhang, X. Wang, X. Jia, P. Xu, M. Zhao and R. Dai, Simultaneous efficient adsorption and photocatalytic degradation of methylene blue over iron(III)-based metal–organic frameworks: a comparative study, *Transition Met. Chem.*, 2019, **44**, 789–797.

42 D. D. Liu, Z. L. Jin, Y. K. Zhang, G. R. Wang and B. Z. Ma, Light harvesting and charge management by Ni_4S_3 modified metal-organic frameworks and rGO in the process of photocatalysis, *J. Colloid Interface Sci.*, 2018, **529**, 44–52.

43 X. Han, D. Y. Xu, L. An, C. Y. Hou, Y. G. Li, Q. H. Zhang and H. Z. Wang, Ni-Mo nanoparticles as co-catalyst for drastically enhanced photocatalytic hydrogen production activity over g-C_3N_4, *Appl. Catal., B*, 2019, **243**, 136–144.